POLITECNICO DI TORINO
Repository ISTITUZIONALE

Sequential solar evaporation and selective lithium extraction enabled by hierarchically porous aerogels with high evaporation rate

Original
Sequential solar evaporation and selective lithium extraction enabled by hierarchically porous aerogels with high evaporation rate / Shi, Q., Zhang, F., Li, J., Gao, F., Guo, Y., Yang, Y., Wang, F., Wang, H., Shi, J., Tiraferri, A., Liu, B.. - In: CHEMICAL ENGINEERING JOURNAL. - ISSN 1385-8947. - 525:521(2025). [10.1016/j.cej.2025.170310]

Availability:
This version is available at: 11583/3005948 since: 2025-12-18T08:19:28Z

Publisher:
Elsevier

Published
DOI:10.1016/j.cej.2025.170310

Terms of use:

This article is made available under terms and conditions as specified in the corresponding bibliographic description in the repository

Publisher copyright
Elsevier postprint/Author's Accepted Manuscript

© 2025. This manuscript version is made available under the CC-BY-NC-ND 4.0 license
http://creativecommons.org/licenses/by-nc-nd/4.0/.The final authenticated version is available online at:
http://dx.doi.org/10.1016/j.cej.2025.170310

(Article begins on next page)

15 November 2026

Revised manuscript (unmarked)

Click here to view linked References

Sequential Solar Evaporation and Selective Lithium Extraction Enabled by Hierarchically Porous Aerogels with High Evaporation Rate

Quanyu Shi[a,b], Feng Zhang[c], Jiazhen Li[c], Feng Gao[c,*], Yujie Guo[a,b], Yushun Yang[a,b], Fang Wang[d], Huan Wang[d], Jialin Shi[d], Alberto Tiraferri[e], Baicang Liu[a,b,*]

[a] State Key Laboratory of Hydraulics and Mountain River Engineering, College of Architecture and Environment, Institute of New Energy and Low-Carbon Technology, Sichuan University, Chengdu, Sichuan 610065, PR China

[b] Yibin Institute of Industrial Technology, Sichuan University Yibin Park, Yibin, Sichuan 644000, PR China

[c] SINOPEC Research Institute of Petroleum Processing Co., Ltd., Beijing 100083, China

[d] China Dongfang Electric Group Co., Ltd, Chengdu, Sichuan 611730, PR China

[e] Department of Environment, Land and Infrastructure Engineering, Politecnico di Torino, Corso Duca degli Abruzzi 24, 10129 Turin, Italy

[*] Corresponding authors: Baicang Liu, E-mail: bcliu@scu.edu.cn; baicangliu@gmail.com; Feng Gao, E-mail: gaofeng.ripp@sinopec.com

Abstract

Solar interface evaporation-assisted resource recovery is among the promising technical solution to the water-energy-resource crisis. However, typically low lithium concentrations in the source solution, e.g., seawater, as well as the dynamic nature of SIE limit the performance of adsorbents. In this study, a "temporal separation" strategy is proposed: the aerogel first concentrates Li^+ by solar-driven evaporation and then captures it through selective adsorption. To achieve this, molybdenum disulfide and lithium ion sieves are encapsulated within acrylamide, forming a hierarchically porous aerogel. This structure enhances solar evaporation for rapid Li^+ concentration, followed by efficient selective adsorption. Under 1-sun irradiation, the aerogel achieves an evaporation rate of 2.58 kg m^{-2} h^{-1} with 90.4% photothermal efficiency in saline solution, maintaining excellent stability over extended operation. Within 72 h, the Li^+ concentration increases fourfold, and the embedded sieves deliver a lithium adsorption capacity of 53.4 mg g^{-1}, with excellent performance retained after 12 cycles. Environmental impact assessment indicates shows lower carbon emissions, energy use, and water footprint than other solar evaporators.

Keywords: Solar interfacial evaporation; Lithium extraction; Life cycle assessment (LCA); Sustainable Resource Recovery

1. Introduction

With the advancement of industry and the global transition to cleaner, low-carbon energy systems, lithium, often referred to as the "white oil of the 21st century," has become a core strategic resource supporting the energy revolution. According to the report from the International Energy Agency (IEA), global lithium demand is projected to rise from 265,000 tons (based on Li_2CO_3) to approximately 498,000 tons by 2050 [1], with 90% of this growth driven by the electric vehicle industry. Currently, the primary sources of Li^+ supply are brine deposits and lithium ores [2, 3], with a global total of around 34 million tons [4]. While these Li^+ reserves are sufficient to meet current market demand, the extraction of Li^+ from such resources involves complex processes and high costs [5], posing challenges in meeting future demand. Seawater is a potential alternative source since it holds vast lithium resources, exceeding 230 billion tons, that is, more than 10,000 times the total land-based reserves [3, 6, 7]. However, the feasibility of efficiently extracting lithium from seawater remains a significant challenge due to low lithium concentration (0.1-0.2 mg L^{-1}) and the high concentration of interfering ions (500-10,000 mg L^{-1}) [8, 9].

Traditional direct lithium extraction methods mainly rely on solvent extraction [10], electrochemical extraction [11, 12], membrane separation [13-16], and electrodialysis [17, 18]. While these methods have addressed selectivity issues to some extent, they still face multiple bottlenecks. Specifically, solvent extraction offers high selectivity but is limited by issues such as impurity co-extraction, environmental risks, and high energy consumption. Electrodialysis faces challenges in ion leakage,

membrane fouling, and high energy consumption. Membrane separation technologies exhibit reduced selectivity in high salinity environments and are affected by concentration polarization and scaling. Electrochemical methods, despite their potential for direct lithium recovery, require substantial external energy input and often produce unwanted by-products, complicating large-scale implementation. In contrast, adsorption methods, due to their low investment, environmental friendliness, and high selectivity, are considered a promising and feasible approach for lithium extraction from seawater [19]. Lithium ion sieves (LISs), primarily derived from lithium titanium oxide (LTO), lithium manganese oxide (LMO), and lithium/aluminum layered double hydroxides (Li/Al-LDHs), have become the primary adsorbents for lithium recovery from brines [20-23]. However, the practical application of powdered LISs is often severely limited due to challenges in deployment and recovery, resulting in unavoidable material waste. Encapsulating LISs within a carrier is an effective approach to address these issues. Hydrogels, with their three-dimensional porous networks, abundant binding sites, and environmental benignity [24-27], have thus emerged as excellent carriers for lithium-ion sieves. Furthermore, most methods treat seawater only as a lithium source, overlooking its equally important role as a vast freshwater reservoir. Therefore, developing a method capable of simultaneously recovering freshwater and efficiently extracting lithium holds great promise [28, 29].

Solar-driven interface evaporation (SIE) enhances water evaporation by concentrating solar energy at the air-water interface, thereby achieving low-carbon seawater desalination and wastewater minimization [30-36]. Moreover, integrating

lithium adsorbents into solar evaporators not only raises their local temperature but also enriches lithium through evaporation [37, 38], thereby accelerating adsorption kinetics and enhancing capture efficiency. For example, Liu et al. reported a photothermal floating mat used for solar-driven lithium extraction [39], which achieved a saturated lithium adsorption capacity of 520 mg m^{-2} under 2-sun irradiation. Wang et al. developed spherical polystyrene microspheres loaded with bifunctional LTO/n-doped mesoporous carbon nanocomposites as micro solar evaporators [40], achieving a two-fold increase in lithium recovery under 1-sun irradiation. Despite recent advances, there remains a clear need for an integrated approach that can simultaneously overcome seawater's low lithium content, ensure selectivity in complex ion matrices, and recover freshwater in a sustainable manner.

Based on these insights, we designed a "temporal separation" strategy to overcome the low lithium concentration barrier in seawater. The idea is to first concentrate lithium ions via solar-driven evaporation and then selectively capture them through embedded adsorbents, achieving both freshwater recovery and lithium extraction in a single system (Scheme 1). To realize this, we developed a hydrogel-based aerogel platform by encapsulating MoS_2 as the photothermal component and H_2TiO_3 (HTO) as the lithium-ion sieve within an acrylamide matrix. The hierarchical porous network ensures rapid water transport, stable evaporation, and effective ion diffusion. In the following sections, we detail the synthesis of this material, characterize its structural and photothermal properties, evaluate its performance in solar evaporation and lithium adsorption. Moreover, the synthesis of photothermal components and adsorbents typically involves

energy-intensive procedures or hazardous chemicals. A quantitative life cycle assessment (LCA) is therefore essential to verify the overall sustainability of the proposed technology. By integrating LCA, we systematically assess the environmental impacts associated with both material synthesis and aerogel utilization, enabling a comprehensive and transparent evaluation of its sustainable resource recovery potential.



Scheme 1. Schematic diagram of the solar evaporation and lithium concentration platform.

2. Experimental methods

2.1. Materials

All chemicals were used as received, without further purification. Titanium dioxide (TiO_2, AR) and lithium carbonate (Li_2CO_3, AR) were purchased from Chengdu Kelong Chemical Co., Ltd. (China). Molybdenum disulfide (MoS_2, <2 μm, AR, ≥99.5%), N,N'-Methylenebisacrylamide (MBA, AR, ≥99.0%), N,N,N',N'-Tetramethylethylenediamine (TMEDA, AR, ≥99.0%), sodium dodecyl sulfate (SDS, AR, ≥99%), and ammonium persulfate ($(NH_4)_2S_2O_8$, AR, ≥99.0%) were obtained from Shanghai Aladdin

Biochemical Technology Co., Ltd. Acrylamide (AM, AR, ≥99%), magnesium chloride ($MgCl_2$, 99.0%), calcium chloride ($CaCl_2$, AR, ≥97.0%), sodium chloride (NaCl, AR, ≥99.5%), potassium chloride (KCl, AR, ≥99.5%), and lithium chloride (LiCl, AR, ≥99%) were purchased from Shanghai Macklin Biochemical Co., Ltd. Hydrochloric acid (HCl, AR, 37%) was supplied by Tianjin Kemeier Reagent Co., Ltd. Deionized water (DI) from a commercial ultrapure water system (Sichuan Youpu Ultrapure Technology Co., Ltd.) was used for all experiments.

2.2. Preparation of H_2TiO_3 (HTO)

Li_2TiO_3 powder was synthesized via a conventional solid-state reaction. Specifically, Li_2CO_3 and TiO_2 with a stoichiometric ratio of Li:Ti = 2:1 were first thoroughly ground and mixed to obtain a homogeneous precursor. The mixture was then transferred to a muffle furnace, where it was calcined at 800 °C for 4 h with a heating rate of 5 °C·min^{-1}. After cooling to room temperature, Li_2TiO_3 powder was obtained. The as-prepared Li_2TiO_3 was subsequently immersed in 0.5 mol L^{-1} HCl solution at 70 °C under gentle stirring for 24 h to ensure complete Li^+/H^+ ion exchange. The resulting solid was washed with deionized water until neutral, followed by freeze-drying, to finally obtain Li_2TiO_3 ion sieves.

2.3. Preparation of MTH hydrogel

MTH was prepared via a cross-linked foaming polymerization method. First, 7.0 g of molybdenum disulfide (MoS_2) was dispersed in 25 mL of deionized water and stirred vigorously for 1 h. To this suspension, 4.2 g of acrylamide (AM) and 0.3 g of N, N'-methylenebisacrylamide (MBA) were added, and the mixture was stirred and sonicated

for 30 min to ensure thorough mixing. Subsequently, 0.06 g of sodium dodecyl sulfate (SDS) was introduced as a pore-forming agent, the suspension was rapidly stirred, and once foaming occurred, TMEDA (1.2 mL) was added as a catalyst; stirring was continued until the foam dissipated. Different amounts of HTO were then added, corresponding to mass fractions of 1.5 wt%, 2.5 wt%, and 3.0 wt%, respectively. The suspension was sonicated to remove air bubbles, after which ammonium persulfate (3.0 mL) was added to initiate cross-linking. The resulting hydrogel was then immersed in deionized water for 24 h to remove residual reagents. The resulting material was first obtained as a hydrogel. After freeze-drying, it was converted into an aerogel (MTH), which was used for structural characterization. Unless otherwise specified, evaporation and adsorption experiments were carried out with the hydrated hydrogel form.

2.4. Characterization

The morphology and elemental composition of the hydrogel were analyzed using scanning electron microscopy (SEM) with energy-dispersive X-ray spectroscopy (EDS). Contact angle was measured by depositing a 2 μL DI water droplet on the hydrogel surface. UV-Vis-NIR measurement tested the transmittance and reflection of MTH hydrogel. Differential scanning calorimetry (DSC) was used to determine evaporation enthalpy (20–100 °C, heating rate5℃ min^{-1}). The chemical composition of hydrogel was analyzed by X-ray photoelectron spectrum (XPS) using a Thermo Scientific: ESCALAB250Xi. Ion concentrations in solution were measured using ICP–OES.

2.5. Swelling measurement

The acrylamide-based hydrogel was submerged in deionized water to assess its swelling behavior. After reaching equilibrium, the swollen hydrogel was carefully taken out, blotted with filter paper to remove excess surface water, and weighed using an electronic balance. The swelling ratio was then determined using the following equation:

$$Swelling\ ratio = \frac{W_2 - W_1}{W_1} \quad \text{(Eq. 1)}$$

where W_1 and W_2 are the weights (g) of the dry hydrogel and swollen hydrogel, respectively.

2.6. Solar steam generation

Solar evaporation experiments with MTH were conducted in a glass vessel containing 80 mL of simulated saline water. The MTH aerogel was cut into 2 × 2 × 2 cm cubes and irradiated under a 1000 W m^{-2} solar simulator at room temperature and a humidity of approximately 50%. During the experiment, mass changes of the system were monitored using an electronic balance, while temperature variations were continuously monitored using an infrared camera. The heat losses calculation in SIE process can be obtained according to supporting information.

2.7. Adsorption efficiency and capacity

20 mg MTH and 20 mL of 100 mg L^{-1} Li^+ solutions were added into plastic centrifuge tube and shaken in a water bath. After reaching the adsorption equilibrium, the supernatant was collected using 0.22 μm filter membrane and the concentration of filtered supernatant was measured by atomic fluorescence spectroscopy. To investigate the profound adsorptions properties of MTH, the effect of pH (7-12), contact time (0-20 h), initial concentration of Li^+ ions (50-300 mg L^{-1}) and temperature (298, 318 K)

was conducted. The removal efficiency (Eq. 2) and the adsorption capacity (Eq. 3) were calculated by the following formula [41, 42]:

$$R_e = \frac{C_0 - C_e}{C_0} \quad \text{(Eq. 2)}$$

$$Q_e = \frac{(C_0 - C_e)}{m} V \quad \text{(Eq. 3)}$$

where R_e (%) and Q_e (mg g^{-1}) represent the removal efficiency and adsorption capacity for the Li^+; C_0 (mg L^{-1}) and C_e (mg L^{-1}) are the initial concentration and the equilibrium concentration of Li^+, respectively; V (L) is the volume of solution; and m (g) is the amount of adsorbent (MTH).

2.8. Adsorption kinetics

To investigate the adsorption processes, the kinetic data were fitted by pseudo-first-order and pseudo-second-order kinetic models. The pseudo-first-order (Eq. 4) and pseudo-second-order models (Eq. 5) were used to analyze and fit the experimental data [43]:

$$\ln(Q_e - Q_t) = \ln Q_e - k_1 t \quad \text{(Eq. 4)}$$

$$\frac{t}{Q_t} = \frac{1}{k_2 Q_e^2} + \frac{t}{Q_e} \quad \text{(Eq. 5)}$$

In which Q_e and Q_t (mg g^{-1}) are the adsorbed amounts of Li^+ on MTH at equilibrium and time t (min); and k_1 (min^{-1}) and k_2 (g (mg h) $^{-1}$) refer to the rate constant of pseudo-first-order and pseudo-second-order models, respectively.

2.9. Adsorption isotherms and thermodynamic study

In order to further study the adsorption behavior and thermodynamic properties, the adsorption performance between MTH and Li^+ were carried out at two different temperatures (293, 313 K) and two well-known models (Langmuir, Freundlich) were

also employed to simulate the adsorption isotherm. The formulas of Langmuir (Eq. 6) and Freundlich models (Eq. 7) are described as follows [29]:

$$Q_{\mathrm{e}} = \frac{Q_{\mathrm{m}} \mathrm{K_L} C_{\mathrm{e}}}{1 + \mathrm{K_L} C_{\mathrm{e}}} \quad (\mathrm{Eq.}\,6)$$

$$\ln Q_{\mathrm{e}} = \frac{1}{\mathrm{n}} \ln C_{\mathrm{e}} + \ln \mathrm{K_F} \quad (\mathrm{Eq.}\,7)$$

where Q_e and Q_m (mg g^{-1}) represent the adsorbed amount of Li^+ ions on MTH at equilibrium and the maximum adsorption capacity; C_e (mg L^{-1}) represents the equilibrium concentration of Li^+ ions; K_L and K_F are the Langmuir and Freundlich constant related to the adsorption capacity; n is relevant to the adsorption intensity.

2.10. Calculation of separation factors

The separation factor (α) in lithium extraction quantifies the selectivity of a lithium-ion sieve (LIS) toward Li^+ over competing cations in a multi-ion system. It is defined as the ratio of the distribution coefficients (K_d) of Li^+ and a competing ion (Me), expressed as [29]:

$$\alpha = \frac{K_d^{Li}}{K_d^{Me}} \quad (\mathrm{Eq.}\,8)$$

where the distribution coefficient (K_d) is given by:

$$K_d = \frac{(C_0 - C_e)V}{C_e m} \quad (\mathrm{Eq.}\,9)$$

C_0 is initial concentration of the ion in solution before adsorption (mg/L); C_e is equilibrium concentration of the ion after adsorption (mg/L); V is the volume of the solution used in the adsorption experiment (L); m is the mass of the LIS adsorbent (g). A higher separation factor (α) indicates stronger Li^+ selectivity, which is critical for efficient lithium recovery from brine solutions containing competing ions.

2.11. Reusability measurement

The regeneration performance of the MTH was evaluated at room temperature. The adsorbent (20 mg) was added to 20 mL of a 100 mg L^{-1} Li^+ solution and allowed to adsorb for 20 h. The adsorbent was then immersed in 50 mL of 0.5 mol L^{-1} HCl solution and shaken at 293 K for 24 hours to facilitate the desorption and regeneration of Li^+. Finally, the adsorbent was washed thoroughly with deionized water and the regenerated hydrogel was used for another adsorption cycle.

3. Results and discussion

3.1. Preparation and characterization of MTH

The MTH hydrogel was prepared by encapsulating HTO and MoS_2 within an AM matrix. MoS_2, with its strong light absorption properties, served as the photothermal component, while HTO functioned as Li^+ adsorbent. SEM images (Fig. 1a-c) showed that the aerogel exhibited a rich macroporous structure, which should facilitate the transport of water to the surface of MTH [44]. Furthermore, incident light can reflect within the abundant pores, thereby promoting effective light transmission and enhancing absorption efficiency [45]. The presence of macropores should also improve the storage capacity, preventing the accumulation of salts on the surface of MTH [46]. SEM-EDS suggested that both Mo and Ti elements were evenly distributed across the aerogel skeleton, indicating the successful integration of MoS_2 and HTO. Nitrogen adsorption-desorption isotherms (Fig. 1d) displayed a type IV profile with an H3 hysteresis loop, consistent with the coexistence of interconnected macropores and mesopores. These results corroborated the effective incorporation of HTO into the matrix, in line with the SEM observations..

The surface hydrophilicity of MTH was evident from the rapid absorption of a water droplet within approximately 1.15 s (Fig. 1e). FTIR spectra (Fig. 1f) revealed characteristic peaks at 1594 cm^{-1}, associated with amide groups (-CONH-), which readily form hydrogen bonds with water molecules. These functional groups contribute to the excellent hydrophilicity of the material and sustain continuous water transport and evaporation [47]. Additional peaks at 2360 cm^{-1} and 2162 cm^{-1} are attributed to the stretching vibrations of C-S and C-N, respectively. An absorption peak at 1992 cm^{-1} was also observed, likely arising from the interaction between the functional groups within the aerogel and MoS_2. The aerogel color also changed from colorless to black upon MoS_2 incorporation, indicating broad solar absorption (Fig. S1). UV-Vis-NIR spectra (Fig. 1g) further confirmed efficient light capture across the solar spectrum.

DSC analysis (Fig. 1h) showed that the evaporation enthalpy of water confined in the hydrogel was lower than that of bulk water, suggesting that water molecules within the polymer network required less energy to vaporize. This effect is attributed to hydrogen bonding and capillary forces within the micro- and nanochannels of the material, which disrupt the bulk water structure. Finally, compression tests (Fig. 1i) indicated that MTH was elastic at strains below 50% and exhibited higher compressive strength at larger strains (>60%), supporting its good mechanical robustness.

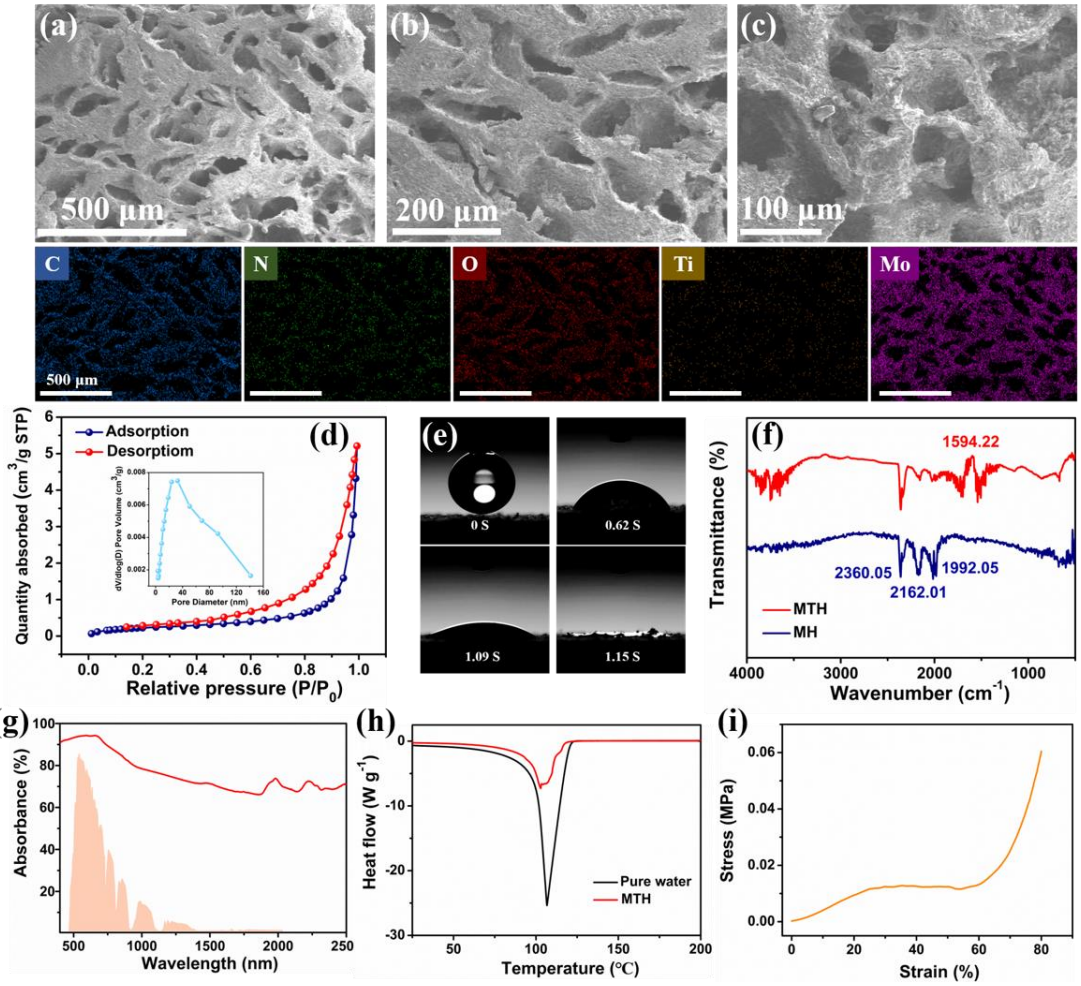


Fig. 1. Characteristics of MTH aerogel/hydrogel. (a-c) SEM images of MTH at different resolutions; (d) Particle size distribution of MTH; (e) Contact angles of water on MTH at different contact times; (f) FTIR spectrum of MTH; (g) UV/Vis-NIR absorption spectrum of MTH; (h) DSC curves of pure water and MTH; (i) Compressive stress-strain curve of MTH.

3.2. Solar-driven water evaporation performance

The solar evaporation performance of MTH was evaluated under a standard solar simulator while mass changes of the brine were recorded with an electronic balance. Additionally, an infrared camera was used to monitor the surface temperature variations during the evaporation process (Fig. 2a). To assess the impact HTO loading, hydrogels containing 0, 1.5, 2.5, and 3.0 wt% HTO were tested under 1-sun irradiation in 3.5 wt%

artificial seawater. The water evaporation rate increased with HTO content up to 2.5 wt% but decreased at 3.0 wt% (Fig. 2b). At 3.0 wt% HTO, the evaporation performance of MTH was lower than that of the HTO-free hydrogel, likely because excess HTO blocked internal pores and hindered water transport. Consequently, subsequent studies utilized MTH containing 2.5 wt% HTO.

The adaptability of MTH was then assessed under different solar intensities of 0.5, 1, and 2 sun. As expected, the evaporation rate rose with increasing intensity, reaching ~3.25 kg m^{-2} h^{-1} at 2 sun (Fig. 2c). The corresponding, average surface temperature also increased with light intensity, stabilizing at 42.5 ℃ under 1 sun after 30 min (Fig. 2d). Thermal imaging confirmed that heat was concentrated at the evaporator surface, with minimal transfer to bulk water (Fig. S2). A photothermal conversion efficiency of 90.4% was calculated, with only 2.0% of the heat dissipated into the brine (Fig. S3).

At approximately 25°C and 45% relative humidity, the water evaporation performance was systematically evaluated under stable solar intensity (1 sun) (Fig. 2e). To isolate the photothermal effect, the dark evaporation background rate of 0.25 kg m^{-2} h^{-1} was subtracted from the total evaporation rate. The evaporation rate of MTH reached 2.5 kg m^{-2} h^{-1}, exceeding that of pure water, and remained above 2.0 kg m^{-2} h^{-1} even after 12 h of continuous operation (Fig. 2g). As the salinity increased from 3.5 wt% to 20 wt% NaCl, the evaporation rate gradually decreased (Fig. 2f), which can be attributed to trace salt precipitation that hinders water transport and vapor escape (Fig. S4).

As reported in previous desalination studies, solar evaporation materials often

accumulate large amounts of salt crystals on their surfaces due to insufficient water supply [48]. This crystal accumulation impairs solar thermal conversion, reduces light absorption, and, in severe cases, blocks the water channels within the hydrogel. Therefore, the salt resistance and self-cleaning performance of MTH were also evaluated. In 20 wt% brine, only minor salt crystals appeared at the edges of MTH after 12 h, with no accumulation in the main evaporation area (Fig. S4). Notably, when a 2 $\times$2 cm^2 piece of MTH was placed in 3.5 wt% brine and 0.5 g of NaCl powder was spread on the surface of the material, the NaCl crystals dissolved and completely disappeared into the saltwater within 210 min under 1 sun irradiation (Fig. S5). This rapid dissolution can be attributed to the uniform distribution of macropores and mesopores within the hydrogel. Due to the retention by the macropores, salt ions do not accumulate on the surface of MTH but instead diffuse downward along the concentration gradient. For comparison, similar evaporators such as squid ink/chitosan required ~8 h for complete salt dissolution under the same conditions [49].

To further evaluate the long-term stability of MTH, a 10-day continuous evaporation test was conducted under 1 sun irradiation in a 3.5 wt% brine (Fig. 2h). The evaporation rate of MTH remained stable throughout, SEM analysis revealed that after prolonged operation, the layered porous network structure of MTH remained intact, with no sign of salt deposition (Fig. S6). Leveraging this evaporation capability, MTH was also tested with a LiCl solution (100 mg L^{-1}) under 1 sun irradiation. After 72 h of evaporation, the concentration of LiCl increased fourfold to approximately 400 mg L^{-1} (Fig. 2i), providing favorable conditions for subsequent lithium extraction.

The practical feasibility of the MTH evaporator is crucial for addressing the global freshwater crisis. To evaluate its seawater desalination performance under real-world conditions, the actual evaporation rate of MTH was tested under natural sunlight using simulated seawater (3.5 wt% NaCl). The device was placed in an open area on the west side of the Environmental Building at Sichuan University in Chengdu, China (Fig. S7). The experiment was conducted from 9:00 to 18:00 on October 15, 2025, with the mass change of water recorded hourly during MTH operation. The solar radiation peaked between 12:00 and 14:00 (≈0.7 kW m^{-2}). As shown in Fig. S7, the MTH evaporator exhibited a rapid increase in evaporation rate under natural sunlight from 10:00 to 14:00, reaching 5.10 kg m^{-2} h^{-1} between 13:00 and 14:00. Remarkably, despite the solar irradiance being only 0.7 kW m^{-2}-lower than that of the laboratory solar simulator (1 sun)-the outdoor evaporation rate exceeded the laboratory value of 2.58 kg m^{-2} h^{-1}. This enhancement can be attributed to lower ambient humidity and higher wind speed in the outdoor environment [50]. The results demonstrate the substantial potential of the MTH hydrogel evaporator for practical seawater desalination applications.

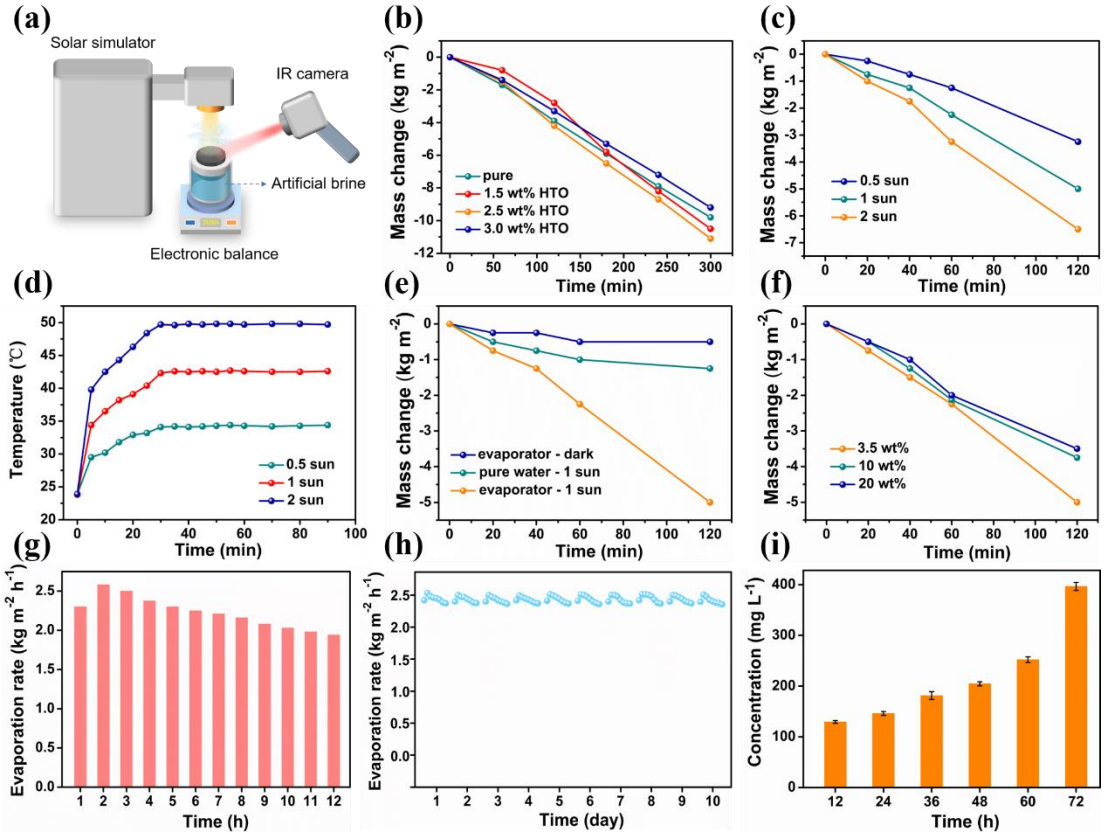


Fig. 2. Solar interface evaporation (SIE) performance and stability of MTH. (a) Schematic diagram of the solar-driven steam generation setup; (b) Mass loss of brine over time with materials characterized by different HTO loadings; (c) Mass loss of brine over time under different solar intensities; (d) Average surface temperature of MTH over time under different solar intensities; (e) Mass change over time of pure water and brine over time under different conditions; (f) Mass change over time of brines with different concentrations; (g) Evaporation rate of MTH during 12 h of continuous operation under 1 sun; (h) Long-term stability test over 10 days under 1 sun; (i) Increase in LiCl concentration for 72 h of evaporation under 1 sun (nominal C_0 = 100 mg L^{-1}). [All the above experiments were conducted under the conditions of a temperature ranging from 25.0 to 25.5 ℃, a humidity of 50 % to 52 %, and a light area of 2×2 cm].

3.3. Li^+ adsorption performance

After Li^+ enrichment by evaporation, the adsorption performance of MTH toward

352 Li^+ was systematically investigated. Since pH plays a critical role in regulating ion-
353 exchange kinetics and stabilizing the structural integrity of the adsorbent, it was first
354 evaluated as a key parameter. As shown in Fig. 3a, the adsorption capacity increased
355 with pH, reaching a maximum of 29.0 mg g^{-1} at pH 12.0 (298 K). This enhancement is
356 primarily attributed to the neutralization of H^+ by OH^-, which facilitates Li^+/H^+
357 exchange in HTO (Eq. S1). Conversely, under acidic conditions, the high concentration
358 of H^+ suppresses adsorption: according to Le Chatelier's principle, excess H^+ drives the
359 equilibrium toward desorption and protonation of exchange sites, reducing accessibility
360 of Li^+ to the HTO lattice. Thus, pH 12.0 was identified as the optimal condition to
361 maximize Li^+ uptake.

362 The effect of contact time on Li^+ adsorption was also investigated. Adsorption
363 capacity increased rapidly in the initial stage and reached equilibrium within
364 approximately 15 h (Fig. 3b). At higher temperatures, the adsorption rate was slightly
365 enhanced, likely due to increased kinetic energy of Li^+ ions and improved diffusion
366 toward active adsorption sites [51]. Kinetic modeling showed that the data fitted well
367 with pseudo-second-order model (R^2=0.996), consistent with chemisorption as the
368 dominant mechanism (Fig. 3c, S8, and Table S2). Equilibrium adsorption studies were
369 conducted using Li^+-concentrated solutions collected after 24 h, 48 h, and 60 h of
370 evaporation. As shown in Fig. 3d, the Langmuir model (R^2=0.993, at 318 K) provided
371 a superior fit compared to the Freundlich model (R^2=0.960, Fig. S9), indicating
372 monolayer adsorption (Table S3). The maximum adsorption capacities of MTH derived
373 from Langmuir fitting were calculated as 36.5 mg g^{-1} (24 h), 49.2 mg g^{-1} (48 h), and

374 53.4 mg g^{-1} (60 h), outperforming many reported adsorbents (Table S4). The desorption
375 efficiency and dissolution loss of MTH are critical factors for evaluating its stability
376 and reusability. The Li^+ desorption efficiency and Ti dissolution loss rate of the MTH
377 hydrogel in 0.5 M HCl were investigated, as shown in Fig. S10. Owing to the excellent
378 memory function of the LIS and its uniform dispersion within the hydrogel [52, 53],
379 MTH achieved a desorption efficiency exceeding 85% and a Ti dissolution loss rate
380 below 0.5% after five cycles. The reduction in Ti dissolution can be attributed to the
381 formation of hydrogen bonds between HTO and the hydrogel matrix, which enhances
382 the interfacial compatibility and structural stability of HTO within the hydrogel [54].
383 To evaluate the adsorption performance under conditions more relevant to pre-
384 concentrated real seawater, additional experiments were conducted at a lower initial Li^+
385 concentration of 5 mg L^{-1}. As shown in Fig. S11, MTH achieved an adsorption capacity
386 of 1.32 mg g^{-1}, validating its potential for real-world applications. Since natural brines
387 typically contain multiple competing ions, particularly Mg^{2+} and Na^+, competitive
388 adsorption tests were performed by introducing Na^+, K^+, Ca^{2+}, and Mg^{2+} into the Li^+
389 solution. MTH showed a clear preference for Li^+ (Fig. 3e), owing to the contribution of
390 HTO. Separation coefficients (Fig. 3f) confirmed strong selectivity of Li^+ over
391 competing cations. The reusability of MTH was assessed through adsorption-
392 desorption cycles using Li^+-concentrated solutions evaporated for 24 h (Fig. S12). Even
393 after 12 successive cycles, MTH retained a high adsorption capacity of 30.7 mg g^{-1},
394 highlighting the structural stability of HTO. Overall, these results demonstrate that
395 MTH combines high adsorption capacity, strong selectivity, and excellent recyclability,

making it a promising candidate for practical lithium recovery from brines.

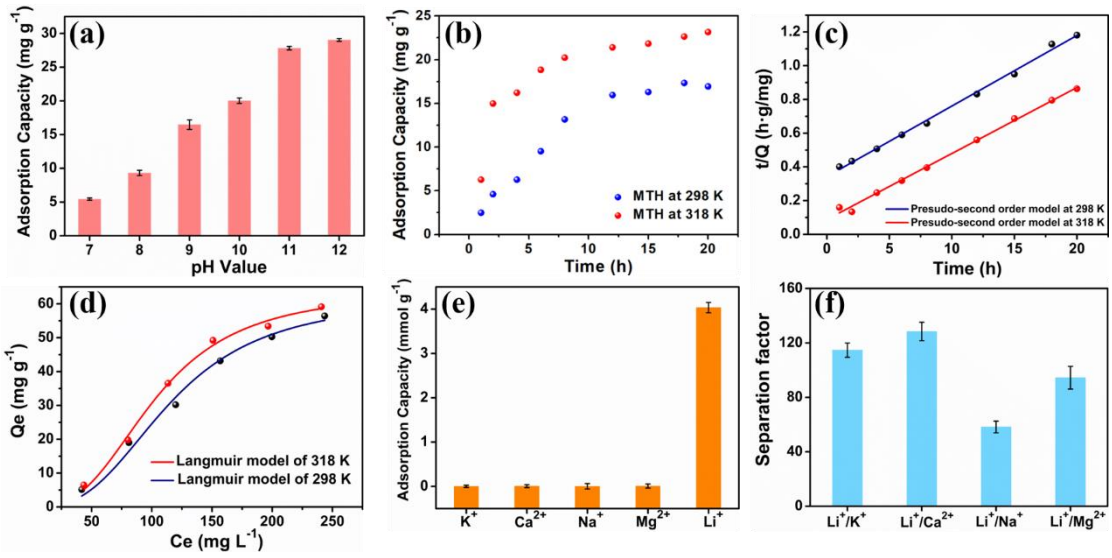


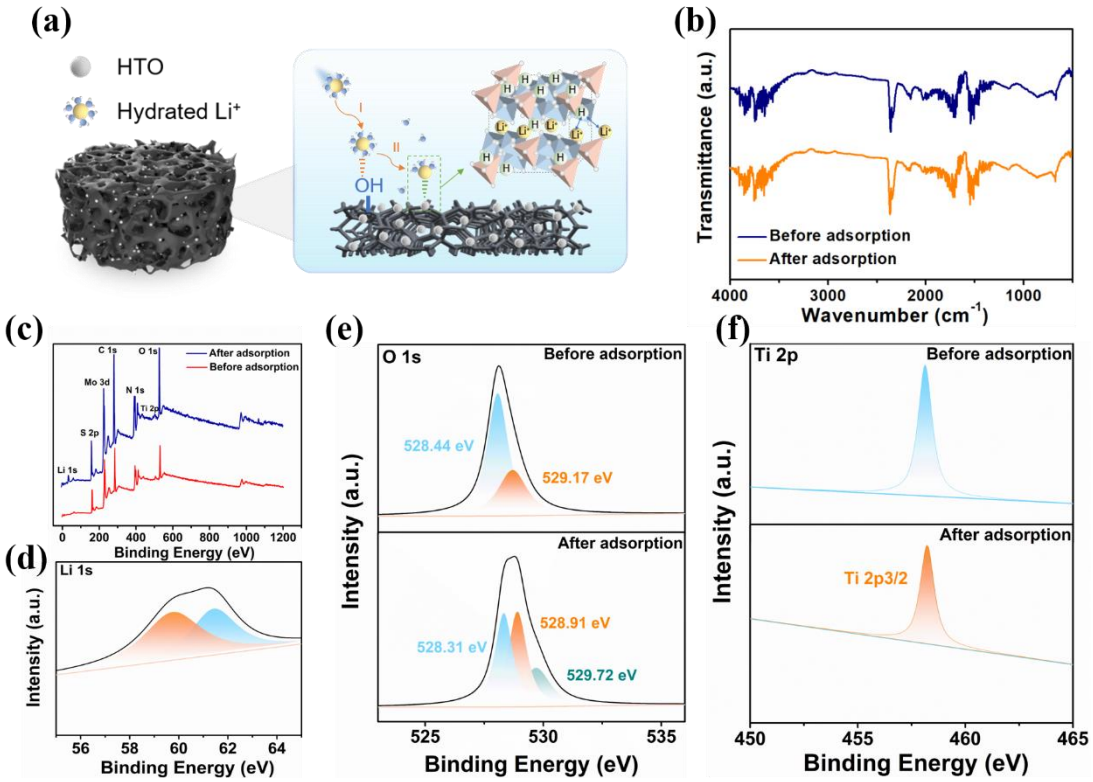
Fig. 3. Lithium adsorption performance of MTH. (a) Effect of pH 7-12 (298 K, C_0=100 mg L^{-1}) on Li^+ adsorption capacity. (b) Adsorption kinetics as a function of contact time (pH 12, C_0=100 mg L^{-1}). (c) Kinetic fitting with the pseudo-second-order model at different temperatures (pH 12, C_0=100 mg L^{-1}). (d) The adsorption capacity of MTH at different Li^+ concentrations (pH 12). (e) Adsorption capacities for Li^+ and competing cations (Na^+, K^+, Ca^{2+}, Mg^{2+}, pH 12, $C_{M^{n+}}$=100 mg L^{-1}). (f) Separation factors of Li^+ relative to other cations.

3.4. Li^+ adsorption mechanism

To elucidate the adsorption mechanism of Li^+ by the MTH hydrogel, a schematic illustration (Fig. 4a) was first employed to visualize the process. The hydrated lithium ions in solution are captured by hydroxyl groups (-OH) within the hydrogel matrix and by hierarchical HTO nanoparticles. The three-dimensional porous network and high hydrophilicity of MTH provide rapid ion transport pathways, facilitating the diffusion of Li^+ toward the adsorption sites. Spectroscopic analyses supported this mechanism. FTIR spectra (Fig. 4b) showed a new vibrational band in the 3600-3900 cm^{-1} region

412 after adsorption, indicating the involvement of hydroxyl groups. Due to the intrinsic
413 selectivity of HTO, the combined action of -OH groups and HTO favored efficient Li^+
414 capture. As hydrated Li^+ ions approach the HTO nanoparticle surface, they initially
415 coordinate with the (1,1,0) and (1,1,1) crystal planes of HTO and subsequently undergo
416 partial dehydration through interactions with lattice hydroxyls [55]. The partially
417 dehydrated Li^+ ions then participate in a solid-state ion-exchange process with
418 structural protons (H^+) in the HTO lattice, forming Li_2TiO_3 (the key process for
419 selective Li^+ capture). The spinel-type framework of HTO provides size- and affinity-
420 based selectivity for Li^+ over other competing cations (Eq. S1). The released H^+ ions
421 migrate into the aqueous phase to maintain charge neutrality. Moreover, adsorption
422 performance is influenced by the density of adsorption sites and the lattice parameters
423 of the adsorbent. The intra-particle diffusion model was also employed to illustrate the
424 internal diffusion mechanism during the adsorption process. As shown in Fig. S13, the
425 adsorption process is divided into three stages: rapid adsorption, intra-particle diffusion,
426 and adsorption equilibrium. In the rapid adsorption stage, the K_1 value is highest,
427 indicating that the adsorption capacity is greatest when Li^+ rapidly adsorbs onto the
428 surface of the hydrogel. During the intra-particle diffusion stage, the Li^+ adsorbed on
429 the MTH surface slowly diffuse into the internal pores. Finally, in the adsorption
430 equilibrium stage, the HTO within the MTH is fully occupied, and the adsorption
431 process halts. To provide further evidence of Li-adsorbent interactions, XPS was
432 conducted before and after adsorption. The survey spectrum (Fig. 4c) showed the
433 appearance of a distinct Li 1s signal after adsorption, which was absent in the pristine

sample. High-resolution Li 1s spectra (Fig. 4d) revealed a new adsorption peak, attributed to the transformation from -OH to Li-O bonding, indicating a change in the electronic environment of lithium and corroborating the ion-exchange mechanism. Similarly, the O 1s spectrum (Fig. 4e) prior to adsorption exhibited two peaks, corresponding to distinct oxygen chemical environments at 528.44 eV and 529.17 eV. Following adsorption, these peaks shifted to 528.31 eV, 528.91 eV, and 529.72 eV, accompanied by an intensity redistribution. These changes reflect alterations in the local oxygen environment induced by Li^+ adsorption. By contrast, the strong peak observed at 458.7 eV in the Ti 2p3/2 spectrum (Fig. 4f) remained unchanged before and after adsorption, indicating that the oxidation state of titanium was preserved, ruling out redox processes and highlighting the ion-exchange nature of the mechanism. Together, these results confirm that Li^+ adsorption by MTH proceeds through a Li^+/H^+ ion-exchange mechanism, mediated by both the HTO lattice and hydroxyl groups in the hydrogel matrix [55].



448

449 Fig. 4. Mechanism of Li^+ adsorption and ion exchange. (a) Schematic diagram of the mechanism of

450 lithium uptake through hydroxyl groups and HTO sites. (b) FTIR spectra before and after Li^+

451 adsorption. (c) XPS survey spectra showing the emergence of a Li 1s signal. (d) High-resolution Li

452 1s spectrum indicating Li-O bonding. (e) O 1s spectra before and after adsorption. (f) Ti 2p3/2

453 spectra showing unchanged titanium oxidation state.

454 ## 3.4. Environmental impact assessment of MTH

455 Life cycle assessment (LCA) has long been a fundamental approach for evaluating

456 the environmental impacts associated with material preparation and utilization [56-58],

457 Our analysis considered multiple categories, including human health, ecosystems, and

458 resource use, using the production of 1 kg of functionalized gel as the reference unit.

459 For benchmarking, MTH was compared with four reported aerogel-based solar

460 evaporators (Table S5) [59-62]. MTH exhibited lower impacts in several key categories.

Global warming potential and water consumption were reduced relative to other evaporators (Fig. 5a, b), largely because the preparation of MTH required only a single soaking step for reagent removal rather than repeated washing with large volumes of deionized water. Terrestrial ecotoxicity was also significantly reduced (Fig. 5c), with environmental burdens more than 95% lower than those of 3D LPE. Stratospheric ozone depletion was mitigated as well (Fig. 5d), since MTH fabrication avoided halogenated solvents and chlorinated reagents commonly used in energy-intensive processes.

Other categories showed similar advantages. MTH demonstrates markedly lower nitrogen emissions to marine ecosystems (Fig. 5e). Nitrogen-related emissions to marine ecosystems were negligible (Fig. 5e) because nitrogen-containing groups were incorporated into the polymer framework without generating liquid effluents. Impacts on human health were also lower: PM2.5 emissions and photochemical oxidant formation were reduced compared with CM-FSS evaporators (Fig. 5f, h). These benefits are attributed to the absence of high-temperature carbonization in MTH synthesis, which otherwise releases particulate matter, and to negligible NO_x emissions compared with evaporators based on nitrogen-containing monomers. The MTH system also demonstrated sustainability in fossil resource consumption (Fig. 5g), underscoring its reduced dependence on fossil fuel energy. Finally, ionizing radiation impacts (Fig. 5i) were diminished relative to other evaporators, consistent with avoidance of energy-intensive separation steps.

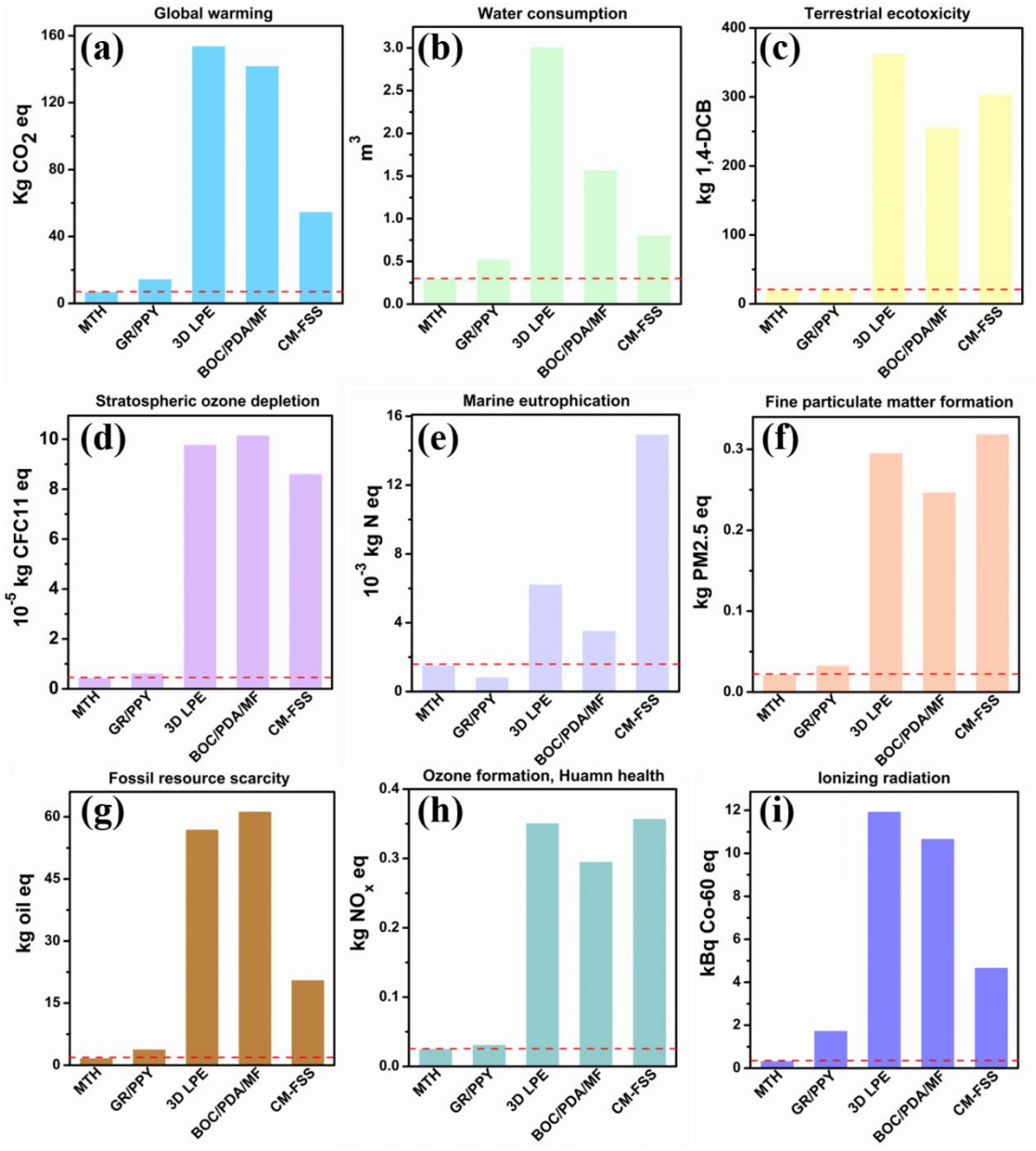


Fig. 5. Life cycle assessment (LCA) comparison of MTH with other reported solar evaporators. Impact categories include (a) global warming potential, (b) water consumption, (c) terrestrial ecotoxicity, (d) stratospheric ozone depletion, (e) marine eutrophication, (f) fine particulate matter formation, (g) fossil resource scarcity, (h) photochemical oxidant formation, and (i) ionizing radiation.

4. Conclusions

This study proposes a “temporal separation” strategy to enhance the synergistic

interaction between solar interface evaporation and lithium extraction. By encapsulating MoS_2 and HTO within an acrylamide matrix, a hierarchical porous aerogel (MTH) was developed, enabling sequential freshwater generation and lithium recovery. The unique macro-mesoporous network structure of MTH ensured the uniform distribution of MoS_2, which efficiently captured solar energy and confined heat at the interface. Under 1 sun irradiation, its evaporation rate reached 2.58 kg m^{-2} h^{-1}, with a photothermal conversion efficiency of 90.4% in 20 wt% brine, maintaining stability over a 10-day period. Additionally, MTH exhibited excellent salt resistance and self-cleaning properties, ensuring continuous operation in high-salinity environments. Importantly, MTH concentrated Li^+ fourfold within 72 h, with embedded HTO providing a high lithium adsorption capacity of 53.4 mg g^{-1}, with excellent reusability over 12 cycles. Beyond performance, LCA confirmed the environmental advantages of MTH. Compared to other solar evaporators, it reduced carbon emissions, energy consumption, and water footprints. Together, these results demonstrate that MTH provides a scalable and sustainable route to harnessing seawater both as a freshwater source and as a lithium resource, contributing to future clean energy supply chains. Although the present study demonstrates the excellent laboratory-scale performance of MTH in sequential solar evaporation and lithium extraction, several aspects should be further considered for large-scale deployment. Firstly, while the constituent materials are low-cost and commercially available, further optimization of synthesis routes will be required to ensure cost-effectiveness at industrial scales. Process intensification and sustainable precursor utilization could further reduce

manufacturing expenses. Secondly, long-term stability under real marine conditions remains a key challenge. The material's mechanical robustness, as evidenced by compression tests, provides a solid foundation; however, its resistance to biofouling, hydrodynamic stress, and prolonged photothermal cycling under natural sunlight must be validated through extended outdoor and oceanic field trials. Thirdly, developing a continuous and self-sustaining operational architecture will be essential for large-scale application. Future system designs may involve modular MTH arrays deployed in solar evaporation ponds or floating marine platforms, integrated with autonomous water supply, in-situ regeneration, and periodic adsorbent recovery mechanisms to enable uninterrupted operation.

Credit authorship contribution statement

Quanyu Shi: Investigation, Methodology, Data curation, Formal analysis, Visualization, Writing–original draft; **Feng Zhang:** Formal analysis; **Jiazhen Li:** Resources; **Feng Gao:** Resources, Writing–review & editing; **Fang Wang** Resources; **Huan Wang** Resources, Writing–review & editing; **Jialin Shi:** Resources, Writing–review & editing; **Yujie Guo:** Formal analysis, Writing–review & editing; **Yushun Yang:** Writing–review & editing; **Alberto Tiraferri:** Validation, Writing–review & editing; **Baicang Liu:** Conceptualization, Supervision, Project administration, Funding acquisition, Writing–review & editing.

Declaration of competing interest

The authors declare that they have no known competing financial interests or personal relationships that could have appeared to influence the work reported in this paper.

Acknowledgements

This work was supported by the National Natural Science Foundation of China (52270075), Outstanding Youth Science Foundation of Sichuan Province Natural Science Foundation (2025NSFJQ0010), and Dongfang Electric Corporation (Dongfang Boiler) University-Enterprise Cooperation Project (24H0846). SINOPEC Research Institute of Petroleum Processing Co., Ltd. University-Enterprise Cooperation Project (24H0803). A.T. acknowledges the support of Politecnico di Torino. The views and ideas expressed herein are solely those of the authors and do not represent the ideas of the funding agencies in any form.

References

[1] P.K. Choubey, K.-S. Chung, M.-s. Kim, J.-c. Lee, R.R. Srivastava, Advance review on the exploitation of the prominent energy-storage element Lithium. Part II: From sea water and spent lithium ion batteries (LIBs), Miner. Eng. 110 (2017) 104-121. https://doi.org/https://doi.org/10.1016/j.mineng.2017.04.008.

[2] R.J. Bowell, L. Lagos, C.R. de los Hoyos, J. Declercq, Classification and Characteristics of Natural Lithium Resources, Elements 16(4) (2020) 259-264. https://doi.org/10.2138/gselements.16.4.259.

[3] J. Hou, H. Zhang, A.W. Thornton, A.J. Hill, H. Wang, K. Konstas, Lithium Extraction by Emerging Metal–Organic Framework-Based Membranes, Adv. Funct. Mater. 31(46) (2021) 2105991. https://doi.org/https://doi.org/10.1002/adfm.202105991.

[4] A. Razmjou, M. Asadnia, E. Hosseini, A. Habibnejad Korayem, V. Chen, Design principles of ion selective nanostructured membranes for the extraction of lithium ions, Nat. Commun. 10(1) (2019) 5793. https://doi.org/10.1038/s41467-019-13648-7.

[5] P.K. Choubey, M.-s. Kim, R.R. Srivastava, J.-c. Lee, J.-Y. Lee, Advance review on the exploitation of the prominent energy-storage element: Lithium. Part I: From mineral and brine resources, Miner. Eng. 89 (2016) 119-137. https://doi.org/https://doi.org/10.1016/j.mineng.2016.01.010.

[6] S. Yang, F. Zhang, H. Ding, P. He, H. Zhou, Lithium Metal Extraction from Seawater, Joule 2(9) (2018) 1648-1651. https://doi.org/https://doi.org/10.1016/j.joule.2018.07.006.

[7] X. He, S. Kaur, R. Kostecki, Mining Lithium from Seawater, Joule 4(7) (2020) 1357-1358. https://doi.org/https://doi.org/10.1016/j.joule.2020.06.015.

[8] O.A. Kazi, W. Chen, J.G. Eatman, F. Gao, Y. Liu, Y. Wang, Z. Xia, S.B. Darling, Material Design Strategies for Recovery of Critical Resources from Water, Adv. Mater. 35(36) (2023) 2300913. https://doi.org/https://doi.org/10.1002/adma.202300913.

[9] P. Srimuk, X. Su, J. Yoon, D. Aurbach, V. Presser, Charge-transfer materials for electrochemical water desalination, ion separation and the recovery of elements, Nat. Rev. Mater. 5(7) (2020) 517-538. https://doi.org/10.1038/s41578-020-0193-1.

[10] Y. Sun, Q. Wang, Y. Wang, R. Yun, X. Xiang, Recent advances in magnesium/lithium separation

and lithium extraction technologies from salt lake brine, Sep. Purif. Technol. 256 (2021) 117807. https://doi.org/https://doi.org/10.1016/j.seppur.2020.117807.

[11] K. Sun, M. Tebyetekerwa, X. Zeng, Z. Wang, T.T. Duignan, X. Zhang, Understanding the Electrochemical Extraction of Lithium from Ultradilute Solutions, Environ. Sci. Technol. 58(8) (2024) 3997-4007. https://doi.org/10.1021/acs.est.3c09111.

[12] Z. Li, I.C. Chen, L. Cao, X. Liu, K.-W. Huang, Z. Lai, Lithium extraction from brine through a decoupled and membrane-free electrochemical cell design, Science 385(6716) (2024) 1438-1444. https://doi.org/10.1126/science.adg8487.

[13] X. Li, M. Xu, X. Liu, Q. She, W.J. Lau, L. Yang, Surface-engineered nanofiltration membranes for sustainable lithium recovery from real brine: Addressing fouling and scaling challenges, Water Res. 278 (2025) 123400. https://doi.org/https://doi.org/10.1016/j.watres.2025.123400.

[14] R. Wang, R. Alghanayem, S. Lin, Multipass Nanofiltration for Lithium Separation with High Selectivity and Recovery, Environ. Sci. Technol. 57(38) (2023) 14464-14471. https://doi.org/10.1021/acs.est.3c04220.

[15] N. Gan, Y. Lin, B. Wu, Y. Qiu, H. Sun, J. Su, J. Yu, Q. Lin, H. Matsuyama, Supramolecular-coordinated nanofiltration membranes with quaternary-ammonium Cyclen for efficient lithium extraction from high magnesium/lithium ratio brine, Water Res. 268 (2025) 122703. https://doi.org/https://doi.org/10.1016/j.watres.2024.122703.

[16] X. Li, Y. Mo, W. Qing, S. Shao, C.Y. Tang, J. Li, Membrane-based technologies for lithium recovery from water lithium resources: A review, J. Membrane Sci. 591 (2019) 117317. https://doi.org/https://doi.org/10.1016/j.memsci.2019.117317.

[17] X. Pang, Y. Tao, Y. Xu, J. Pan, J. Shen, C. Gao, Enhanced monovalent selectivity of cation exchange membranes via adjustable charge density on functional layers, J. Membrane Sci. 595 (2020) 117544. https://doi.org/https://doi.org/10.1016/j.memsci.2019.117544.

[18] H. Huang, Z. Li, Z. Li, B. Khan, K.-W. Huang, Z. Lai, J.-H. He, Photoelectrochemical lithium extraction, Nano Energy 115 (2023) 108683. https://doi.org/https://doi.org/10.1016/j.nanoen.2023.108683.

[19] T. Ryu, Y. Haldorai, A. Rengaraj, J. Shin, H.-J. Hong, G.-W. Lee, Y.-K. Han, Y.S. Huh, K.-S. Chung, Recovery of Lithium Ions from Seawater Using a Continuous Flow Adsorption Column

602 Packed with Granulated Chitosan–Lithium Manganese Oxide, Ind. Eng. Chem. Res. 55(26) (2016)
603 7218-7225. https://doi.org/10.1021/acs.iecr.6b01632.
604 [20] J. Zhong, S. Lin, J. Yu, Li+ adsorption performance and mechanism using lithium/aluminum
605 layered double hydroxides in low grade brines, Desalination 505 (2021) 114983.
606 https://doi.org/https://doi.org/10.1016/j.desal.2021.114983.
607 [21] X. Zhao, X. Zhang, X. Xing, F. Bian, X. Gao, B. Liu, S. Song, Y. Zhang, H. Huang,
608 Constructing Angstrom-Level Ion Pocket Array in 1D Channel Wall for Efficient Lithium Ion
609 Sieving, Adv. Funct. Mater. 35(10) (2025) 2416628.
610 https://doi.org/https://doi.org/10.1002/adfm.202416628.
611 [22] Z. Han, S. Qi, M. Fu, L. Han, C. Hong, Z. Shen, X. Wang, K. Su, X. Xue, B. Zhang, J. Gu, H.
612 Ma, A Scalable Route to Constructing Hydrogel-Encapsulated Lithium-Ion Sieves-Based
613 Photothermal Fabric Adsorbent for Solar-Enhanced Lithium Extraction from Seawater, Adv. Funct.
614 Mater. 35(25) (2025) 2422901. https://doi.org/https://doi.org/10.1002/adfm.202422901.
615 [23] K. Chen, L. Li, B. Li, Y. Yang, K. Zhu, J. Zhang, Simultaneous Fresh Water Collection and Li+
616 Selective Adsorption Enabled by A Salt-Resistant Separated Solar Evaporator, Adv. Funct. Mater.
617 34(37) (2024) 2402221. https://doi.org/https://doi.org/10.1002/adfm.202402221.
618 [24] S. Guo, Y. Zhang, Z. Yu, M. Dai, X. Liu, H. Wang, S. Liu, J.J. Koh, W. Sun, Y. Feng, Y. Chen,
619 L. Yang, P. Sun, G. Lu, C. Yu, W. Chen, S. De Wolf, Z. Wang, S.C. Tan, Leaf-based energy
620 harvesting and storage utilizing hygroscopic iron hydrogel for continuous power generation, Nat.
621 Commun. 16(1) (2025) 5267. https://doi.org/10.1038/s41467-025-60341-z.
622 [25] S. Guo, Y. Zhang, S.C. Tan, Device design and optimization of sorption-based atmospheric
623 water harvesters, Device 1(4) (2023) 100099.
624 https://doi.org/https://doi.org/10.1016/j.device.2023.100099.
625 [26] S. Guo, S. Patel, J. Wang, Z. Yu, H. Qu, S. Zhang, K. Yu, S. Liu, J.J. Koh, X.Q. Koh, Z.-E. Ooi,
626 D.H.L. Seng, W. Sun, L. Yang, Y. Zhang, J. Wang, S.K. Ravi, C. Yu, S.C. Tan, Self-powered green
627 energy–harvesting and sensing interfaces based on hygroscopic gel and water-locking effects, Sci.
628 Adv. 11(27) eadw5991. https://doi.org/10.1126/sciadv.adw5991.
629 [27] S. Guo, S. Zhang, H. Li, S. Liu, J.J. Koh, M. Zhou, Z. Sun, Y. Liu, H. Qu, Z. Yu, Y. Zhang, L.
630 Yang, W. Chen, C. He, C. Lee, D. Mao, S.K. Ravi, Y. Lai, S.C. Tan, Precisely manipulating polymer

chain interactions for multifunctional hydrogels, Matter 8(4) (2025) 101785. https://doi.org/https://doi.org/10.1016/j.matt.2024.06.024.

[28] S. Mousavinezhad, S. Nili, A. Fahimi, E. Vahidi, Environmental impact assessment of direct lithium extraction from brine resources: Global warming potential, land use, water consumption, and charting sustainable scenarios, Resour. Conserv. Recy. 205 (2024) 107583. https://doi.org/https://doi.org/10.1016/j.resconrec.2024.107583.

[29] B. Liu, Y. Yang, M. Zhou, T. Wang, Y. Liu, Y. Shen, Q. Zhao, X. He, Y. Ma, W. Que, Solar-Driven Dual-functional Adsorvaporator Enabling Efficient Lithium Concentration and Freshwater Generation with Life Cycle Assessment Evaluation, Small 21(32) (2025) 2505347. https://doi.org/https://doi.org/10.1002/smll.202505347.

[30] B. Liu, Y. Yang, Q. Zhao, Y. Liu, Y. Shen, Y. Ma, W. Que, The route for applied interfacial solar vapor generation: fundamental principles, device design, and practical application, Energ. Environ. Sci. 18(13) (2025) 6366-6437. https://doi.org/10.1039/D5EE01542A.

[31] Y. Xiao, H. Guo, M. Li, J. He, X. Xu, S. Liu, L. Wang, T.D. James, Strategies for enhancing the photothermal conversion efficiency of solar-driven interfacial evaporation, Coordin. Chem. Rev. 527 (2025) 216378. https://doi.org/https://doi.org/10.1016/j.ccr.2024.216378.

[32] X. Wu, Y. Lu, X. Ren, P. Wu, D. Chu, X. Yang, H. Xu, Interfacial Solar Evaporation: From Fundamental Research to Applications, Adv. Mater. 36(23) (2024) 2313090. https://doi.org/https://doi.org/10.1002/adma.202313090.

[33] K. Mao, Y. Zhang, S.C. Tan, Functionalizing solar-driven steam generation towards water and energy sustainability, Nat. Water 3(2) (2025) 144-156. https://doi.org/10.1038/s44221-024-00363-x.

[34] H. Zhang, S. Zhou, H. Liu, Z. Qian, X. Wang, All-Weather Solar-Powered Desalination and Synchronous Cs+ Extraction for Salt-Lake Water Enabled by Crown-Ether-Decorated Phase-Change Microcapsules, Adv. Funct. Mater. 34(48) (2024) 2408269. https://doi.org/https://doi.org/10.1002/adfm.202408269.

[35] Z. Yuan, C. Du, L. Qiao, J. Qiao, T. Ye, A. Huang, H. Liu, G.-Z. Yin, X. Wang, Solid-liquid phase change materials for solar-driven interfacial evaporation: Principles, design optimization, and emerging advances in sustainable seawater desalination, Chem. Eng. J. 516 (2025) 164024.

https://doi.org/https://doi.org/10.1016/j.cej.2025.164024.

[36] H. Shen, Z. Zheng, H. Liu, X. Wang, A solar-powered interfacial evaporation system based on MoS2-decorated magnetic phase-change microcapsules for sustainable seawater desalination, J. Mater. Chem. A 10(48) (2022) 25509-25526. https://doi.org/10.1039/D2TA07353F.

[37] H.-B. He, Y. Ma, Q.-K. Zhu, T.-T. Li, C.-W. Lou, J.-H. Lin, H.-T. Ren, Solar-driven Janus fabric evaporator: Efficient desalination and selective lithium enrichment, Chem. Eng. J. 519 (2025) 165433. https://doi.org/https://doi.org/10.1016/j.cej.2025.165433.

[38] Z. Zhou, H. Wang, Q. Li, R. Gao, K. Feng, R. Pan, J. Qu, J. Gong, R. Niu, Solar-driven pump for simultaneous lithium capture and freshwater generation from salt-lake brine, J. Mater. Sci. Technol. 254 (2026) 299-306. https://doi.org/https://doi.org/10.1016/j.jmst.2025.07.054.

[39] X. Chen, W. Yu, Y. Zhang, C. Huang, L. Nie, J. Yu, Y. Zhang, C. Zhang, W. Zhai, X. Zhang, Y. Yu, W. Liu, Solar-Driven Lithium Extraction by a Floating Felt, Adv. Funct. Mater. 34(28) (2024) 2316178. https://doi.org/https://doi.org/10.1002/adfm.202316178.

[40] Q. Xia, Z. Deng, S. Sun, W. Zhao, J. Ding, B. Xi, G. Gao, C. Wang, Solar-enhanced lithium extraction with self-sustaining water recycling from salt-lake brines, P. Natl. A. Sci. 121(23) (2024) e2400159121. https://doi.org/10.1073/pnas.2400159121.

[41] M. Li, Q. Shi, N. Song, Z. Chen, L. Wang, T.D. James, Self-Assembled Artificial Light-Harvesting System Constructed Using Electrostatic Interactions in Aqueous Solution for the Sensing of Heavy Metal Cations, Adv. Opt. Mater. 11(15) (2023) 2203079. https://doi.org/https://doi.org/10.1002/adom.202203079.

[42] M. Li, X. Li, M. Xu, B. Liu, M. Yang, Z. Chen, T. Gao, T.D. James, L. Wang, H. Xiao, A ratiometric fluorescent hydrogel of controlled thickness prepared continuously using microtomy for the detection and removal of Hg(II), Chem. Eng. J. 426 (2021) 131296. https://doi.org/https://doi.org/10.1016/j.cej.2021.131296.

[43] M. Li, M. Yang, B. Liu, H. Guo, H. Wang, X. Li, L. Wang, T.D. James, Self-assembling fluorescent hydrogel for highly efficient water purification and photothermal conversion, Chem. Eng. J. 431 (2022) 134245. https://doi.org/https://doi.org/10.1016/j.cej.2021.134245.

[44] Q. Huang, X. Liang, X. Zhang, C. Yan, J. Liang, H. Tang, Y. Liu, Efficient-heat-utilization 3D T-shaped porous sponge assists 2D photothermal films to achieve self-acting salt rejection and extra

689 evaporation under high-concentration brine, Desalination 499 (2021) 114806.
690 https://doi.org/https://doi.org/10.1016/j.desal.2020.114806.
691 [45] G. Ni, G. Li, Svetlana V. Boriskina, H. Li, W. Yang, T. Zhang, G. Chen, Steam generation under
692 one sun enabled by a floating structure with thermal concentration, Nat. Energy 1(9) (2016) 16126.
693 https://doi.org/10.1038/nenergy.2016.126.
694 [46] Y. Guo, F. Zhao, X. Zhou, Z. Chen, G. Yu, Tailoring Nanoscale Surface Topography of
695 Hydrogel for Efficient Solar Vapor Generation, Nano Lett. 19(4) (2019) 2530-2536.
696 https://doi.org/10.1021/acs.nanolett.9b00252.
697 [47] P. Liu, Y.-b. Hu, X.-Y. Li, L. Xu, C. Chen, B. Yuan, M.-L. Fu, Enhanced Solar Evaporation
698 Using a Scalable MoS2-Based Hydrogel for Highly Efficient Solar Desalination, Angew. Chem. Int.
699 Edit. 61(37) (2022) e202208587. https://doi.org/https://doi.org/10.1002/anie.202208587.
700 [48] Z. Xu, X. Ran, D. Wang, M. Zhong, Z. Zhang, High efficient 3D solar interfacial evaporator:
701 Achieved by the synergy of simple material and structure, Desalination 525 (2022) 115495.
702 https://doi.org/https://doi.org/10.1016/j.desal.2021.115495.
703 [49] X. Liu, Y. Tian, Y. Wu, A. Caratenuto, F. Chen, S. Cui, J.A. DeGiorgis, Y. Wan, Y. Zheng,
704 Seawater desalination derived entirely from ocean biomass, J. Mater. Chem. A 9(39) (2021) 22313-
705 22324. https://doi.org/10.1039/D1TA05068K.
706 [50] J. Jin, C. Wang, D. Wei, B. Wang, X. Lin, W. Zhang, C. Shi, Z. Zhao, L. Wang, F. Wang, An
707 Extremely Salt-Resistant Hydrogel-Based Solar Evaporator for Stable Saturated Brine Desalination,
708 Small 21(15) (2025) 2411624. https://doi.org/https://doi.org/10.1002/smll.202411624.
709 [51] M. Li, B. Liu, Z. Liu, Y. Xiao, H. Guo, Z. An, L. Wang, T.D. James, Reducing Heat Conduction
710 Enhances the Photothermal Efficiency of Upcycled Adsorbents, Adv. Funct. Mater. 33(4) (2023)
711 2209987. https://doi.org/https://doi.org/10.1002/adfm.202209987.
712 [52] L. Tang, S. Huang, Y. Wang, D. Liang, Y. Li, J. Li, Y. Wang, Y. Xie, W. Wang, Highly Efficient,
713 Stable, and Recyclable Hydrogen Manganese Oxide/Cellulose Film for the Extraction of Lithium
714 from Seawater, ACS Appl. Mater. Interfaces 12(8) (2020) 9775-9781.
715 https://doi.org/10.1021/acsami.9b21612.
716 [53] X. Zhang, J. Wu, Y. He, C. Zhao, M. An, L. Li, Porous polyvinyl alcohol/polyacrylamide
717 hydrogels loaded with HTO lithium-ion sieves for highly rapid and efficient Li+ extraction,

718 Desalination 580 (2024) 117587. https://doi.org/https://doi.org/10.1016/j.desal.2024.117587.
719 [54] J. Miao, K. Zhao, F. Guo, L. Xu, Y. Xie, T. Deng, Novel LIS-doped mixed matrix membrane
720 absorbent with high structural stability for sustainable lithium recovery from geothermal water,
721 Desalination 527 (2022) 115570. https://doi.org/https://doi.org/10.1016/j.desal.2022.115570.
722 [55] B. Zhao, Z. Qian, Y. Qiao, J. Li, Z. Wu, Z. Liu, The Li(H2O)n dehydration behavior influences
723 the Li+ ion adsorption on H4Ti5O12 with different facets exposed, Chem. Eng. J. 451 (2023)
724 138870. https://doi.org/https://doi.org/10.1016/j.cej.2022.138870.
725 [56] X. Zhao, H. Zhang, K.-Y. Chan, X. Huang, Y. Yang, X. Shen, Tree-Inspired Structurally Graded
726 Aerogel with Synergistic Water, Salt, and Thermal Transport for High-Salinity Solar-Powered
727 Evaporation, Nano-Micro Lett. 16(1) (2024) 222. https://doi.org/10.1007/s40820-024-01448-8.
728 [57] Y. Kuang, C. Chen, G. Chen, Y. Pei, G. Pastel, C. Jia, J. Song, R. Mi, B. Yang, S. Das, L. Hu,
729 Bioinspired Solar-Heated Carbon Absorbent for Efficient Cleanup of Highly Viscous Crude Oil,
730 Adv. Funct. Mater. 29(16) (2019) 1900162. https://doi.org/https://doi.org/10.1002/adfm.201900162.
731 [58] Y. Zhang, S. Jia, X. Yuan, L. Ding, T. Ai, K. Yuan, W. Wang, L. Magagnin, Z. Jiang, High-
732 efficiency removal of Pb (II) and Cu (II) by amidoxime functionalized silica aerogels: Preparation,
733 adsorption mechanisms and environmental impacts analysis, Sep. Purif. Technol. 335 (2024)
734 126079. https://doi.org/https://doi.org/10.1016/j.seppur.2023.126079.
735 [59] S. Yan, H. Song, Y. Li, J. Yang, X. Jia, S. Wang, X. Yang, Integrated reduced graphene
736 oxide/polypyrrole hybrid aerogels for simultaneous photocatalytic decontamination and water
737 evaporation, App. Catal. B: Environ. 301 (2022) 120820.
738 https://doi.org/https://doi.org/10.1016/j.apcatb.2021.120820.
739 [60] J. Ma, L. An, D. Liu, J. Yao, D. Qi, H. Xu, C. Song, F. Cui, X. Chen, J. Ma, W. Wang, A Light-
740 Permeable Solar Evaporator with Three-Dimensional Photocatalytic Sites to Boost Volatile-
741 Organic-Compound Rejection for Water Purification, Environ. Sci. Technol. 56(13) (2022) 9797-
742 9805. https://doi.org/10.1021/acs.est.2c01874.
743 [61] Q. Gan, Y. Xiao, C. Li, H. Peng, T. Zhang, M. Ye, g-C3N4/MoS2 based floating solar still for
744 clean water production by thermal/light activation of persulfate, Chemosphere 280 (2021) 130618.
745 https://doi.org/https://doi.org/10.1016/j.chemosphere.2021.130618.
746 [62] D. Yang, Y. Guo, Z. Yu, Z. Jiang, W. Xiang, X. Wu, J. Wang, Surface Oxygen Vacancy

747 Engineering for Enhanced Volatile Organic Compounds Removal in Solar-Interfacial Water
748 Evaporation, Environ. Sci. Technol. 59(14) (2025) 7117-7128.
749 https://doi.org/10.1021/acs.est.4c14436.

750